Symmetry breaking in $Ge_{1-x}Mn_xTe$ and the impact on thermoelectric transport

Journal Name

Symmetry breaking in $Ge_{1-x}Mn_xTe$ and the impact on thermoelectric transport[†]

Jesse Adamczyk,[a‡] Ferdaushi A. Bipasha,[b‡], Grace Rome,[a] Kamil Ciesielski,[a] Elif Ertekin,[b] Eric S. Toberer[*a]

Germanium telluride is a high performing thermoelectric material that additionally serves as a base for alloys such as GeTe-AgSbTe₂ and GeTe-PbTe. Such performance motivates exploration of other GeTe alloys in order understand the impact of site substitution on electron and phonon transport. In this work, we consider the root causes of the high thermoelectric performance material $Ge_{1-x}Mn_xTe$. Along this alloy line, the crystal structure, electronic band structure, electron and phonon scattering all depend heavily on the Mn content. Structural analysis of special quasirandom alloy structures indicate the thermodynamic stability of the rock salt phase over the rhombohedral phase with increased Mn incorporation. Effective band structure calculations indicate band convergence, the emergence of new valence band maxima, and strong smearing at the band edge with increased Mn content in both phases. High temperature measurements on bulk polycrystalline samples show a reduction in hole mobility and a dramatic increase in effective mass with respect to increasing Mn content. In contrast, synthesis as a function of tellurium chemical potential does not significantly impact electronic properties. Thermal conductivity shows a minimum near the rhombohedral to cubic phase transition, while the Mn_{Ge} point defect scattering is weak as indicated by the low K_L dependence on Ge-Mn fraction (Figure 10). From this work, alloys near this phase transition show optimal performance due to low thermal conductivity, moderate effective mass, and low scattering rates compared to Mn-rich compositions.

1 Introduction

Alloying enables concurrent tuning of electronic, thermal, and mechanical properties; as such, chalcogenide semiconductor alloys have a rich history of achieving excellent thermoelectric performance. For example, the alloy $(GeTe)_{85}(AgSbTe_2)_{15}$ (TAGS) has been used on NASA's multi-mission radioisotope thermoelectric generator (MMRTG) program for powering Mars rovers. Along with TAGS, other GeTe alloys have also emerged, such as $Ge_{1-x}Pb_xTe$[1,2] and GeTe-Bi₂Te₃[3–5] with excellent thermoelectric performance. The rock salt $Ge_{1-x}Mn_xTe$ solid solution is particularly interesting due the change in crystal structure from the GeTe and MnTe end-members, the potential impact of high-spin d^5 Mn^{2+}, and the known high thermoelectric performance. More generally, it is quite unusual for a IV-VI compound to show improved thermoelectric properties when alloyed with a $3d$ transition metal. In this study, we combine theory and experiment to investigate the fundamental electron and phonon transport as a function of both Te and Mn composition.

Considering the phase diagram of the GeTe-MnTe pseudobinary, both GeTe and MnTe undergo a transition to the rock salt crystal structure at elevated temperature (Figure 1a). This leads to a continuous solid solution between these two binary compounds at high temperature. However, at low temperature, two additional crystal structures emerge. For GeTe at low temperature, a rhombohedral structure (Figure 1b) forms that can be thought of as a rock salt structure whose symmetry is broken by a $2°$ skewing of the cubic unit cell angles (ferroelectric phase transition).[7,8] In contrast, MnTe forms in the NiAs structure, where the Mn cation retains its 6-fold bonding. Considering the low temperature alloy space, the addition of Mn to rhombohedral GeTe decreases the distortion, ultimately yielding the rock salt structure at ∼20% MnTe mole fraction near room temperature. Between ∼20%–50% MnTe near room temperature, this rock salt phase is stable and a two phase region emerges for compositions between 50-92% Mn. It is possible to achieve Mn compositions above 50% in the rock salt structure by quenching from high temperatures. Considering the end members of the alloy, GeTe and MnTe have drastically different native electronic properties that nevertheless

[a]*Department of Physics, Colorado School of Mines, Golden Colorado, USA*
[b]*Department of Mechanical Science and Engineering, University of Illinois Urbana-Champaign, Urbana, Illinois 61801, USA*
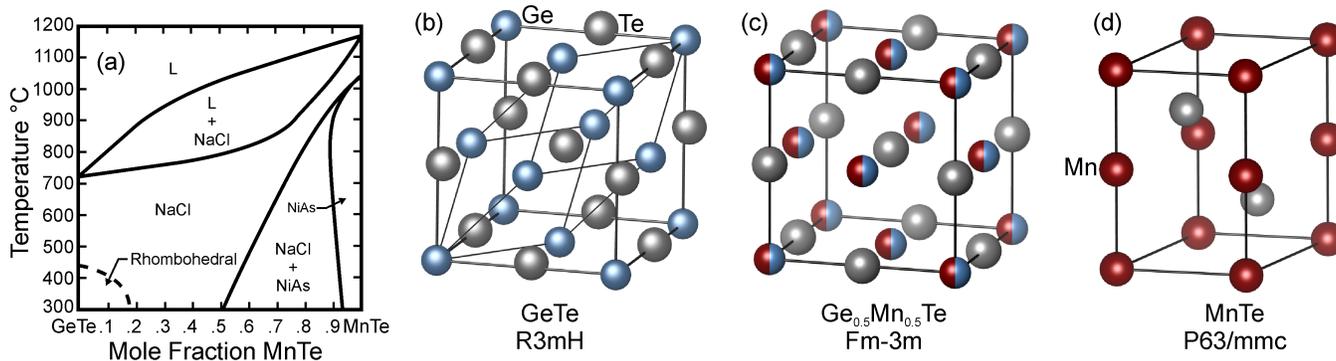
Fig. 1 High temperature phase diagram for the GeTe-MnTe pseudobinary line[6] shows the rhombohedral GeTe structure, (b), followed by a wide cubic rock salt structure, (c). A miscibility gap exists between the rock salt and NiAs structures. Single phase hexagonal NiAs structure, (d), is found at high concentrations of MnTe.

enable high thermoelectric performance in both cases. GeTe has a band gap of $0.5\,eV$[9] and a high hole carrier concentration in the $10^{20}\,h^{+}cm^{-3}$ range as a result of the low formation energy of the Ge vacancies. Much like SnTe, GeTe remains germanium (cation) deficient, even when synthesized in germanium rich conditions, leading to degenerate semiconducting behavior.[10] The high Seebeck coefficient ($\sim 150\,\mu V/K$), relative to the high carrier concentration and mobility ($\sim 55-95\,cm^2/V\cdot s$), allows GeTe to achieve a thermoelectric figure of merit (zT) close to 1 at $650\,K$.[11,12]

MnTe, on the other hand, has a band gap of $1.3\,eV$[13] and an intrinsic carrier concentration in the mid $10^{18}\,h^{+}cm^{-3}$ range and a mobility less than $5\,cm^2/V\cdot s$, leading to high resistivity values at room temperature.[14] MnTe requires high temperatures to activate carriers such that the resistivity can be reduced to a useful level. As the resistivity is reduced, the Seebeck coefficient remains high ($\sim 350\,\mu V/K$) while the total thermal conductivity drops near the amorphous limit ($\sim 0.6\,W/mK$), enabling a zT of 0.6 at $800\,K$.[14–17] The lattice thermal conductivities of both GeTe and MnTe are dominated by Umklapp scattering, leading to high temperature lattice thermal conductivity values less than 1 W/mK.

To date, work within the $Ge_{1-x}Mn_xTe$ single phase region has achieved carrier concentration control through doping and Mn incorporation. The presence of Ge vacancies causes a high hole carrier concentration that can be reduced using Sb and Bi doping of the Mn/Ge cation site. These dopants reduce the hole carrier concentration, improve the Seebeck coefficient, and reduce the lattice thermal conductivity, leading to a zT near unity at high temperature. Counter to Sb and Bi doping, Mn incorporation is found to decrease the cation to anion ratio in $Ge_{1-x}Mn_xTe$, leading to a higher hole carrier concentration in Mn rich samples.[11]

The mobility of GeTe is more than an order of magnitude greater than the mobility of MnTe, however, the density of states effective mass values for these pure compounds are not drastically different (1.4 vs 5.6 m_e). Further investigation reveals that the moderately large GeTe density of states mass is due to significant band degeneracy.[11] In contrast, the individual MnTe bands are quite flat and the compound has a valence band edge degeneracy of two (as well as a different crystal structure). Additionally, the effective mass of the alloys are quite sensitive to

Mn-content. For example, 15% and 50% Mn samples were found to exhibit effective masses of 6.2 and 7.8 m_e, respectively.[11,14,18] Aside from electronic property tuning, estimation of the minimum lattice thermal conductivity of these alloys suggests that there is still room for performance improvements through atomic disorder and microstructure engineering.

Inspired by the excellent performance of $Ge_{1-x}Mn_xTe$, we focus herein on fundamental questions at the intersection of alloy chemistry, structure, and transport properties. We begin by studying the structural transformation for $Ge_{1-x}Mn_xTe$ for x=0.1–0.66. By varying the Te concentration as well, the invariant points of the single phase region are identified, enabling a phase boundary mapping study of the native defects. High temperature measurements of electronic properties (resisitivity, Seebeck coefficient, Hall coefficient) are analyzed as a function of Mn concentration. Single parabolic band analysis allows for the underlying transport parameters (e.g. effective mass, mobility, charge carrier scattering rate) to be determined. Computational modeling of disordered alloys reveals how the electronic structure and scattering rate evolves with composition. By uniting these theoretical predictions with experiment, a cohesive understanding of the complex charge and heat transport in $Ge_{1-x}Mn_xTe$ begins to emerge.

2 Methods

2.1 Synthesis

Synthesis was performed by traditional solid state chemistry techniques that the thermoelectric community is familiar with.[19] Mn pieces (Alfa, 99.999%), Ge ingots (Indium Corp., 99.999%) and Te shot (5NPlus, 99.999%) were used as precursors elements for synthesis. Elements were weighed by hand to an accuracy of +/- 1 mg and ball milled using tungsten carbide ball milling vials (SPEX 8004). Ball milling was performed for 1.5 hours under a nitrogen atmosphere using a SPEX 8000D high energy milling machine. After milling, powder was removed from the ball mill vials and sealed under vacuum in fused silica ampoules. Ampoules were annealed for 24 hours at $550\,°C$. After ball milling, powders were sieved through $106\,\mu m$ sieves and loaded into graphite dies. The powders were consolidated into $12.7\,mm \times 2\,mm$ pellets by pressing in a home-built vacuum hot press at $823\,K$ for 12 hours.[20]

2.2 Measurement

Seebeck measurements were performed using a custom-built measurement apparatus[21]. The Seebeck coefficients were measured from 323-623 K with 2 heating and cooling cycles performed to identify any sample evolution during measurements. Resistivity measurements from 323-623 K were done using a 4-point Van der Pauw probe geometry on a custom-built apparatus. Density of the samples were obtained using geometric measurements and an analytical balance. Thermal diffusivity measurements were performed on a Netzsch LFA 467 Flash Diffusivity measurement system. Conversion from thermal diffusivity to thermal conductivity utilized the equation $\alpha = \frac{\kappa}{dc_p}$ where α is thermal diffusivity, d is density, and c_p is the heat capacity obtained by the Dulong-Petit approximation.

Hall carrier concentration and mobility measurements were performed using a custom-built apparatus[22] with a magnetic field value of 1.0 T. Measurements were only performed at room temperature. X-Ray diffraction was performed using a Bruker D2 Phaser with a $\theta - 2\theta$ geometry. Rietveld refinements on the XRD patterns were performed using TOPAS V6 Academic.[23] SEM imaging with energy-dispersive spectroscopy (EDS) was performed using an FEI Quanta 600i SEM. Grain sizes of the samples were determined from 5 images at 5 different locations on each sample and the averaged data is shown in ESI Table 2. For each phase in the sample, EDS measurements were taken at 5 different locations on the samples with the averaged ternary compositions shown in ESI Figures 13–33.

2.3 Computational Methods

To understand the configurational thermodynamics of the $Ge_{1-x}Mn_xTe$ alloys, the special quasirandom structures (SQS) formalism[24] in combination with first-principle calculations were utilized. SQS represent configurations of alloys for which correlations in atomic configurations most closely mimic those of purely random alloys.[24] The alloy theoretical automatic toolkit (ATAT)[25] was used to generate the structures with the mcsqs code[26]. The SQS are constructed from 64 atom supercells for both rhombohedral and rock salt, for compositions $Ge_{1-x}Mn_xTe$ with x= 3.125, 6.25, 9.375, 12.5, 15.625, 18.875, 21.925, 25.0, 28.125, 31.25, 37.5, 43.75, 50.0%. These 13 different compositions correspond to the experimentally measured range. When generating SQS, pairs and triplets were taken into account with radii large enough to include three and four nearest neighbor atoms. The Monte Carlo algorithm for SQS generation was executed until the objective function improvement stopped, which resulted in a very similar objective function for all generated structures. For each composition, the objective function was matched closely with the case of a random alloy.

First-principles total energy calculations are carried out via density functional theory within the generalized gradient approximation of the Perdew-Burke-Eznerhof (PBE)[27], as implemented in the Vienna Ab-initio Simulation Package (VASP)[28]. Core and valence electrons are treated with a projector augmented wave (PAW) formalism[29]. The plane wave sets were truncated at a constant energy cutoff of 500 eV and a Γ-centred K-mesh of 3x3x3
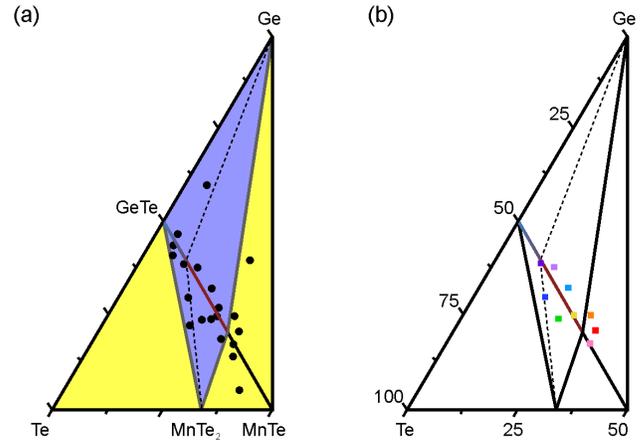
Fig. 2 (a) The Te-Ge-MnTe phase diagram is dominated by the iso-electronic alloy extending from GeTe. This alloy creates two broad two-phase regions (purprle) extending to Ge and MnTe$_2$. The rhombohedral to cubic transition occurs at intersection of the two dashed lines. Yellow triangles represent 3-phase regions while black dots indicate samples prepared to confirm the as-shown phase diagram. (b) Colored squares identify samples used for electronic property measurements. The temperature dependent transport measurements shown later in the text have a consistent color scheme with these points.

was used to perform the relaxation. All structures were fully relaxed with respect to internal degrees of freedom until the forces on all atoms were less than 1 meV/Å. An onsite Hubbard U, with $U = 4$ eV, was included to account for the localized 3d electrons present in Mn. A U parameter of 4 eV based on analysis from prior literature.[30,31] The effect of U on the position and shape of the VBM, and hence the conclusions drawn here, appears to be modest. Even so, we include U = 4 eV in our work due to the improved description of Mn 3d localized orbitals, degree of Mn 3d – Te 5p hybridization, and a more accurate description of the MnTe band gap (see ESI figure 10). Spin-polarized calculations were performed, with an initial magnetization of 5 μ_B to each Mn. Ferromagnetic and antiferromagnetic spins were both tested, and the antiferromagnetic orientations were found to be energetically favourable in the SQS (similar as the antiferromagnetic ordering present in MnTe). Therefore, the results are shown for the antiferromagnetic spin configurations. In all cases we obtain a magnetic moment of 4.5 μ_B for Mn atoms, consistent with Mn species in $3d^5$ high spin configuration.

3 Results & Discussion

3.1 Phase Equilibria

The processing times and techniques in the Methods section resulted in polycrystalline samples with large average grain sizes (5–19μm range, ESI Table 2). X-ray analysis shows that the samples are either rhombohedral or rock salt GeTe solid solution, depending on Mn content and that the impurity phase concentrations range from 40% to phase pure for all samples including those used for phase boundary identification (Figure 2a, ESI Figures 13–23). The presence of impurity phases is intentional, as such phases pin the elemental chemical potentials and thereby control the native defect concentrations. Numerous studies high-
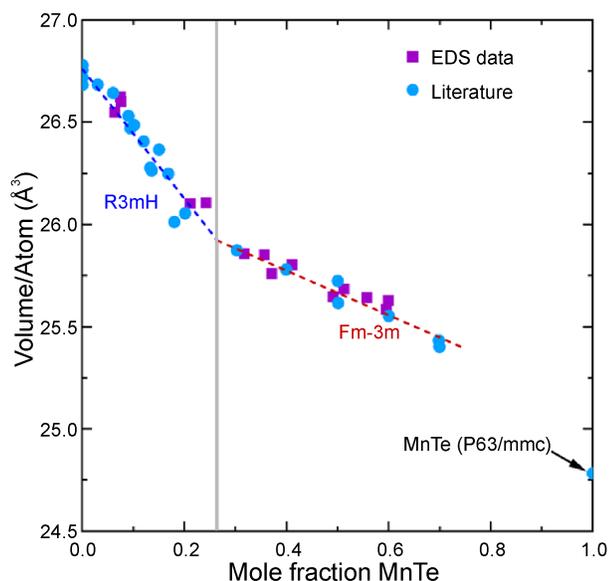
Fig. 3 The volume per atom of the structures along the GeTe-MnTe pseudobinary line shows deviations from Vegard's law due to changes in both crystal symmetry and overall atomic arrangements. The transition point from rhombohedral to cubic is ~26% MnTe.

light the process and importance of phase boundary mapping using impurity phases.[32–36]

The high intensity and sharpness of the X-ray diffraction peaks (ESI Figures 13–33) indicates that the thermal treatment was sufficient to bring samples to an equilibrium state suitable for further characterization. Phase fractions acquired from Rietveld refinements can be found in ESI Table 2. EDS measurements of the compositions indicate that the resulting samples have retained their nominal composition during the synthesis and processing into dense pellets (ESI Figures 13–33). The samples have densities >94% after hot pressing into polycrystalline disks. At this density, the minor fractions of intragranular porosity will have a negligible effect on transport properties (see ESI Figure 30 for an effective medium approximation for spherical inclusions[37]).

Based on the secondary phases observed, we proposed Figure 2 as the phase diagram for the Mn-deficient component of Ge-Mn-Te phase diagram. The diagonal line spanning GeTe–MnTe corresponds to Figure 1a, showing a single phase region that transitions from rhombohedral to rock salt. This understanding of the transition across the phase boundary is supported by X-ray diffraction patterns and SEM (ESI Figures 13–33) of samples within the GeTe-Ge$_{0.5}$Mn$_{0.5}$Te-Ge and GeTe-Ge$_{0.5}$Mn$_{0.5}$Te-MnTe$_2$ phase regions. In these blue regions, we observe the presence of only two phases even though there are three structures (rocksalt, rhombohedral, and diamond-Ge or pyrite-MnTe$_2$) at the vertices of the triangles. Samples prepared in these regions exhibit secondary phases of either elemental Ge and MnTe$_2$. The remaining yellow regions of Figure 2a are three phase regions (Te-MnTe$_2$-GeTe; MnTe$_2$-MnTe-Ge$_{0.5}$Mn$_{0.5}$Te; Ge$_{0.5}$Mn$_{0.5}$Te-Ge-MnTe).

To determine when the rhombohedral to cubic transition occurs in our samples, we consider the volume per atom from X-ray diffraction refinement. Figure 3 shows data collected from the

literature[6,11] as well as our own refinements; collectively, these indicate two linear regimes that transition in slope at approximately 26%. These results are consistent with Figure 1a, and indicate that the rock salt phase is not being quenched into samples with low Mn content. In contrast to this non-diffusive transition, the partitioning of Mn-rich alloys to MnTe is limited during cooling. Nonequilibrium rock salt structured samples were produced with Mn contents up to 59%; considering Figures 1a and 3, an anneal temperature of 1073 K would achieve an Mn content of 70% in the rock salt structure. The single phase rock salt phase region extends all the way to MnTe at high temperature (Figure 1a); however, significant variation in lattice parameter values (not shown in 3) from literature[6,38,39] suggest it is challenging to quench MnTe into the rock salt structure.

SEM micrographs of the samples found in ESI Figures 13–33 support the existence of the phase boundary edges shown in Figure 2. While many of the samples in ESI Figures 13–33 show significant fractions of secondary phases, the electronic property measurements were performed on samples ESI Figure 13–23. In most of these samples, the concentration of secondary phases is close to 10%, however, the samples Mn$_{0.2}$Ge$_{0.225}$Te$_{0.575}$ and Mn$_{0.16}$Ge$_{0.3}$Te$_{0.54}$ have impurity phase concentrations of MnTe$_2$ of up to 40%. At this high concentration, MnTe$_2$ is contributing significantly to the conduction and measured properties of the samples.

3.2 Electronic Properties

Mn content in Ge$_{1-x}$Mn$_x$Te increases the resistivity by a full order of magnitude as shown in Figure 4a. Prior literature shows a similar increase in resistivity driven by Mn in the same composition range.[11,18] The root causes of the increase in resistivity due to Mn content will be developed below through a combination of Hall effect measurements and alloy first principles calculations. In contrast to the effect of Mn content, tellurium concentration is found to have no effect – samples on either side of the Ge$_{1-x}$Mn$_x$Te phase boundary do not show distinguishable differences in resistivity from one another.

The electronic properties in Figure 4b highlight the impact of temperature on the charge carrier transport properties of the Ge$_{1-x}$Mn$_x$Te samples. Resistivity is found to weakly increase with increasing temperature, growing by ~1 mΩ-cm across the full temperature range for all samples. This slope is consistent with the high temperature resistivity trends of GeTe and other degenerate thermoelectrics such as SnTe and PbTe.[40,41] Based on these consistent slopes but changing resistivities, it is inferred that the residual resistivity changes. The samples with the highest residual resistivity values are all manganese rich while the low residual resistivity samples are manganese deficient.

Beyond the overall magnitude and slope of the resistivity curves, samples rich in GeTe undergo a rhombohedral to cubic transition at high temperature, but the structural change shows no discernible impact on the electrical resistivity. We do not expect there to be major changes in the resistivity as a function of structure as the defects driving electronic transport are not expected to change significantly. Slight decreases in resistivity at
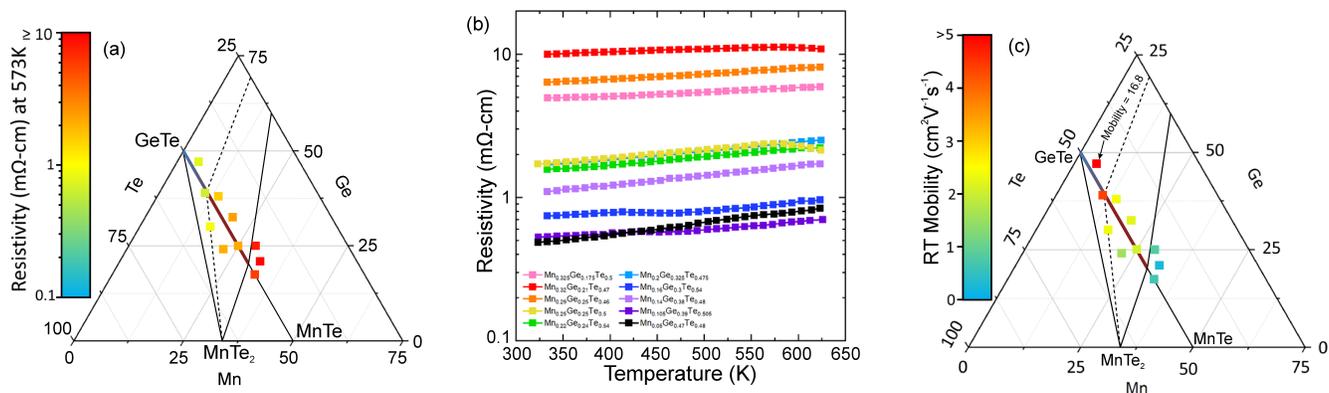
Fig. 4 (a) Composition dependent heat map of The resistivity shows an order of magnitude difference across the $Ge_{1-x}Mn_xTe$ alloy. Panel (a) shows the high temperature (573 K) dependence on composition while (b) shows the temperature dependent resistivity curves indicates extrinsic semiconductor behavior. (c) Room temperature mobility decreases with higher Mn content and is comparatively insensitive to Te content.

high temperatures are likely a result of impurity phases (ESI Figures 13–33) dissolving and precipitating in and out of the matrix phase.

At room temperature, Hall measurements indicate that Mn has only a limited effect on the hole carrier concentration with all of the carrier concentration values between 10^{20}–10^{21} h^+cm^{-3}. In $Ge_{1-x}Mn_xTe$, both Mn and Ge behave as 2+ cations resulting in isoelectronic substitutions that, to first order, should not affect the carrier concentration. Based on prior work on GeTe, it is known that V_{Ge} defects are the primary source of holes and such cation vacancies are expected to continue in this solid solution.[3] The carrier concentration of MnTe is significantly less (10^{18} h^+cm^{-3}) and the change in crystal structure to hexagonal NiAs-type is expected to significantly alter the energetics of cation vacancy formation. Other literature[11] suggests that the carrier concentration slightly increases with increasing Mn content, however, the data in ESI Figure 1 does not support this trend.

Hole mobility is highest near GeTe ($17 \, cm^2/V \cdot s$) and decreases to below $1 \, cm^2/V \cdot s$ with increasing Mn content (Figure 4c). This order of magnitude change in hole mobility drives the changes in electrical resistivity shown in Figure 4a. These mobility measurements alone do not distinguish the relative impact of changes in effective mass and charge carrier scattering.

High temperature Seebeck coefficients in Figure 5a are found to be consistent with the degenerate resistivity and carrier concentration values. Samples with the highest Seebeck coefficients have the highest resistivity values and vice versa. All samples' Seebeck coefficients are found to increase moderately with temperature, suggesting single parabolic band behavior of the samples. At temperatures above 550 K the decrease in slope of the high temperature Seebeck coefficients is evidence of the onset of minority carrier activation. Higher temperatures will likely result in a decreasing Seebeck coefficient as cross gap activation continues to occur. Concentration dependent Seebeck coefficients at 573 K (Figure 5b) show how the Mn concentration dramatically increases the Seebeck coefficient from near $100 \, \mu V/K$ to greater than $225 \, \mu V/K$. Such a change in Seebeck coefficient would normally be a result of carrier concentration effects, however, the

hole concentrations in ESI Figure 1 are relatively unchanging. This increase in Seebeck coefficients supports the notion that Mn is altering the electronic band structure.

A density of states effective mass was determined by approximations of the single parabolic band model assuming acoustic phonon scattering.[42,43] It should be noted that the single parabolic band model does not necessitate single nor parabolic bands to analyze electronic properties in a useful manner.[19] Acoustic phonon scattering was chosen as the dominant scattering mechanism for consistency with prior literature.[11,18] Hole effective mass at room temperature (Figure 5c) dramatically increases from near $1 \, m_e$ on the Ge rich side to greater than $12 \, m_e$ for Mn rich samples. Based on calculations, it is suggested that the effective mass increases because of simultaneous flattening and smearing of the valence band.[11]

3.3 Structural Stability and Bond Length Distribution

Having established key features of the $Ge_{1-x}Mn_xTe$ alloy, we now turn to first principles to explore the effects of alloying on the stability, coordination environment, and effective band structure. In Figure 6(a) we probe the evolution of the crystal structure with increasing Mn incorporation. The supercells are initialized in the low symmetry rhombohedral GeTe structure, but allowed to fully relax during geometry optimization. In rhombohedral GeTe, angles α, β, and γ between lattice vectors are all equivalent, $\sim57.8°$. For supercells with low Mn these angles remain close to $\sim57.8°$ during relaxation, but as x increases the angles approach $60°$, indicating a transformation to the rock salt phase. Some variability in the relationship between angles α, β, γ and x is expected due to configurational disorder, however the trend shown is consistent with the experimentally observed transformation to rock salt with added Mn. We observe that the transformation occurs more smoothly and slowly in the first-principles simulations than in experiment. Additionally, as shown in the inset, the volume change also varies more smoothly, without an obvious change in slope as in Figure 3.

From the relaxed SQS, it is possible to gain additional insights
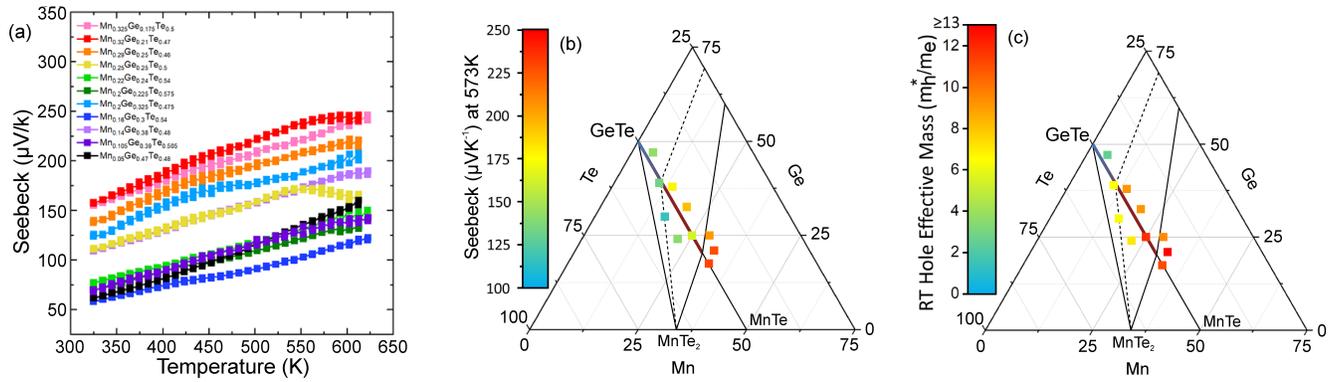
Fig. 5 (a) The Seebeck coefficients rise nearly linearly with temperature, as expected for heavily doped semiconductors. (b) Increasing Mn content is found to increase the Seebeck coefficient at high temperature. (c) The hole effective mass (300 K) increases dramatically with an increase in Mn.
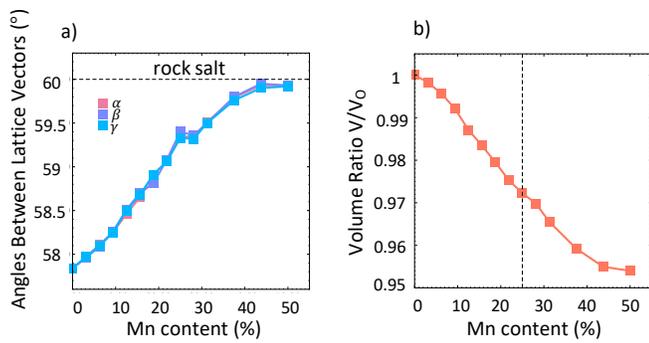
Fig. 6 (a) With increasing Mn content, the angles between supercell lattice vectors for fully relaxed alloy supercells smoothly converge to the high symmetry rock salt value. (b) The relative change in the volume varies smoothly with increasing x.

Fig. 7 The bond length distributions in SQS supercells for $Ge_{1-x}Mn_xTe$ alloys of varying composition. Metallic blue and maroon colors show the distribution of the Ge-Te and Mn-Te bond lengths respectively. As the degree of Mn incorporation increases, first the Mn-Te and eventually the Ge-Te bond lengths shifts from a bimodal distribution (indicating the short and long bonds of the rhombohedral phase) to a single peak at an intermediate bond length (indicating the high symmetry rock salt phase).

into the appearance of rock salt phase by identifying patterns in the bond length distribution as Mn is incorporated (Figure 7(a)). In GeTe, the low temperature rhombohedral phase is stabilized by the lone pair of s electrons present on the Ge^{2+} cation.[44] The stereochemical activity of the lone pair drives the symmetry-breaking distortion and off-centric coordination around Ge, resulting in asymmetric octahedra with three long (3.24 Å) and three short (2.84 Å) Ge-Te bonds around each Ge. In rock salt GeTe, however, the longer bonds are shortened and the shorter bonds are lengthened, resulting in six equal bonds (3.00 Å) and symmetric octahedra with 180° bond angles. Similarly, for MnTe in the hexagonal NiAs structure, we find the bond lengths are 2.98 Å.

The bond length distributions of the fully relaxed $Ge_{1-x}Mn_xTe$ SQS with x= 0, 6.25, 18.75 and 50.0% and MnTe are plotted in Figure 7. The bond length distribution with increasing x also shows a smooth evolution. As Mn is incorporated, the tendency for off-centering becomes reduced due to the lack of lone pairs on the Mn cations. For instance, at 6.25% Mn incorporation, the Ge-Te bond lengths remain largely distributed around their rhombohedral values, while the Mn-Te bond lengths cluster into two distinct groups with more similar bond lengths (~ 2.9 Å and ~ 3.1 Å) – both cations locally still exhibit an off-centric coordina-

tion. As the Mn content further increases to 18.75% and 50%, the Mn-Te bonds quickly become pulled inwards and no longer form two distinct groups, but instead are centered around 2.98 Å with a wide distribution. Like the Mn-Te bonds, the Ge-Te bonds also become pulled inwards and more symmetric with increasing Mn, but they do so more slowly – even at $x = 50\%$, they still show a fairly wide distribution. Compared to the Mn-Te bonds, the Ge-Te bonds more strongly resist the formation of a symmetric arrangement, which is reasonable given the lone pair of s electrons present on Ge.

3.4 Band Structure Evolution

Next, we explore how the incorporation of Mn and the associated change in crystal structure affects the electronic band structure. While previous work on the electronic structure of (Ge,Mn)Te has focused on the band structure of GeTe supercells with one or two Mn atoms substituted[11,45], it is of interest to explore the electronic structure of fully disordered $Ge_{1-x}Mn_xTe$ alloys. The band structures of the alloy supercells exhibit band folding, making them difficult to compare with the primitive cell band structure of the parent compound. Therefore, we use band unfolding[46] to project the supercell band structures back to the primitive unit cell for the parent rock salt and rhombohedral phases. This approach enables us to generate 'renormalized' band structures for each composition, to systematically analyze their evolution with Mn inclusion. The spin up and spin down polarizations are not distinguishable from each other, so we show only one spin in the 'renormalized' band structure. The band unfolding was performed using the BandUP code[47,48].

We calculated the band structure of pure GeTe and disordered alloy SQS $Ge_{1-x}Mn_xTe$ with x= 3.125, 6.25, 9.375, 12.5, 15.625, 18.875, 21.925, 50%. Distinct from the results shown in Figures 6 and 7, here the SQS are initialized in rhombohedral and rock salt phases, and during the geometry optimization the supercell lattice vectors remain fixed while internal atomic coordinates are allowed to relax. This way, we freeze the lattice vectors into well-defined rhombohedral or rock salt structures, which makes it easier to unfold the SQS band structures and compare them to each other. For a given composition x, the unfolded band structures for the rhombohedral and rock salt phases therefore represent two possible extremes from one end of the structural transformation to the other, while for intermediate values of x the actual band structure most likely lies somewhere in between.

The renormalized band structures for rhombohedral and rock salt supercells are shown in Figure 8. The rhombohedral phases in Figure 8(a-d) are shown for compositions where they are experimentally observed, for $x = 0\%$, 6.25%, 12.5%, and 18.75%. The rock salt phases in Figure 8(e-h) are shown for compositions of $x = 18.75\%$, 21.88% and 50%, where they are experimentally observed, as well as at 0% as a reference for comparison. For rock salt, we show the unfolded band structure using the Brillouin zone path of the rhombohedral phase. Since the rock salt structure is a higher symmetry version of the rhombohedral structure, several segments of the low symmetry path become equivalent such as $B_1 \rightarrow L \rightarrow \Gamma$ and $B \rightarrow Z \rightarrow \Gamma$. These degeneracies highlight a key aspect of the rock salt phase, namely, the greater degree of band degeneracy arising from the higher symmetry. Showing both structures along the same path more clearly illustrates the evolution of the band structure with increasing Mn as the structural transformation occurs.

Beginning with the rhombohedral systems, the band structure for pure GeTe (Figure 8a), obtained from unfolding the band structure of a GeTe supercell, recovers the typical expected dispersion for GeTe. It shows an indirect gap of 0.56 eV, with VBM at Σ (between P to Γ) and CBM at L, in agreement with prior DFT results[49,50]. Figure 8(b-d) show how the band structure evolves

at $x = 6.25\%$, 12.50%, and 18.75% Mn. The color bar (shown in a non-uniform scale to highlight differences) indicates the spectral weight (number of bands present) at each k-point and energy window. Even at 6.25% Mn inclusion, the effect of alloying is evident. The alloy retains the key features of the band structure of GeTe, but the sharp bands become smeared and broadened. As Mn incorporation acts as an extrinsic perturbation to the periodicity of pure GeTe, the reduced spectral weight and the smeared, broadened bands reflect the loss of the Bloch character of the states. The ghost-like flat bands that emerge around energies 5 eV below the Fermi energy are the filled $3d^5$ states of the Mn impurities, while the unfilled $3d$ orbitals appear near the conduction band minimum.

We also observe that broadening induced by the inclusion of $x = 6.25\%$ Mn causes the peaks at points L and Z to slightly extend upwards towards the VBM, resulting in a greater convergence of extrema at the valence band edge. In pure GeTe the energy offset between VBM Σ and the peak at L is around 0.17 eV. The energy offset to Z is 0.23 eV, and to the peak along $\Gamma - X$ is 0.45 eV. At 6.25% Mn content, these energy differences decrease respectively to 0.11, 0.11, and 0.21 eV respectively. All three bands are converged within an energy window of $\approx$100 meV at 12.5% Mn content (Figure 8c). The observed band convergence offers an explanation for increased Seebeck in alloyed rhombohedral systems for $x = 10\%$-15%, and may be associated with the increased symmetry as the structure evolves towards the rock salt phase. At 18.75% Mn content, the VBM appears shifted from Σ to between Z-Γ path, with an $\sim$30 meV energy difference between these two points. This change is also consistent with transition to rock salt, for which the VBM occurs at Z.

Figure 8(e-h) shows unfolded band structures for compositions $x =$0%, 18.75%, 21.88%, and 50%, now for the rock salt phase. In rock salt GeTe (shown for reference), the VBM and CBM both occur at L and Z, which are now degenerate by symmetry. However the peak in the VBM at Σ is only 0.08 eV lower in energy. The band structure for rock salt at 18.75% (Figure 8f) is similar to that of rhombohedral at the same composition (Figure 8d), but the bands are even more well converged. The higher band degeneracy arising from increased symmetry points to an underlying explanation for the increased Seebeck with Mn shown in Figure 5. With further increasing x, the bands become more smeared, and even begin to express features associated with the band structure of rock salt MnTe (see ESI Figure 7). Even so, the nominally degenerate paths $B_1 \rightarrow L \rightarrow \Gamma$ and $B \rightarrow Z \rightarrow \Gamma$ show differences in spectral weights, which arise from local structural variations (bond angles and lengths that retain features of the rhombohedral phase, especially around Ge atoms). In spite of the band convergence, we also note the flattening and spreading of the VBM extrema with Mn inclusion. The curvature of the bands at Σ, which is between K to Γ in rock salt k-path is reduced by a factor of three at 12.5% Mn inclusion, and six at 18.75% Mn alloying, compared to rock salt GeTe (ESI Figure 8). Details of the approach used to estimate curvatures for the unfolded band structures are given in the ESI (see ESI Figure 8). The DOS plots and the trends in DOS effective mass for both rhombohedral and rocksalt phase are shown in the ESI (ESI Figure 11 and 12). At 50-50 composition the tops of
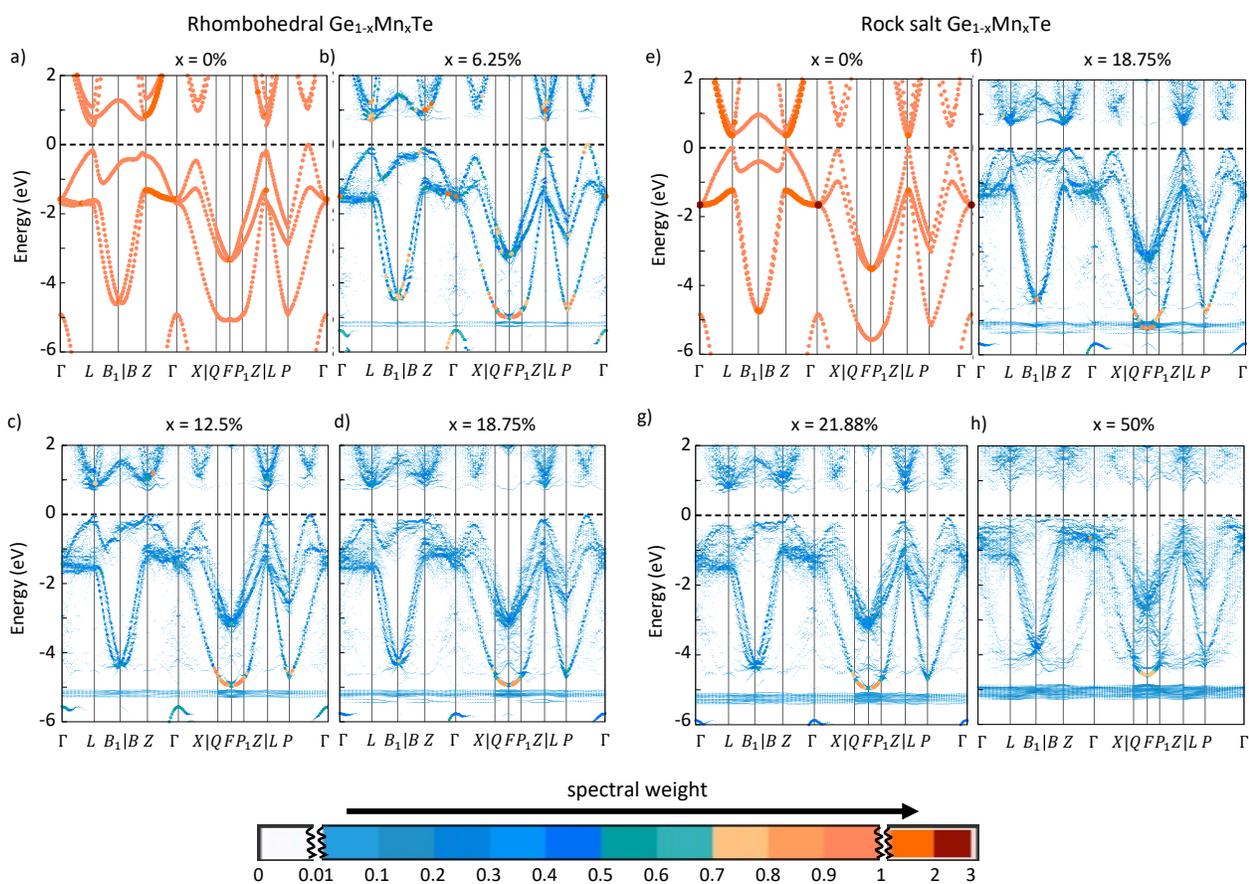
Fig. 8 The band structure SQS alloy structures $Ge_{1-x}Mn_xTe$ evolve significantly with both symmetry (rhombohedral and rock salt) and composition. For ease of comparison, the Brillouin zone path plotted for the high symmetry rock salt corresponds to the same path shown for the lower symmetry rhombohedral phase. Due to the higher symmetry of rock salt, the following segments are degenerate: $B_1 \rightarrow L \rightarrow \Gamma$ and $B \rightarrow Z \rightarrow \Gamma$, $F \rightarrow P_1$ and $F \rightarrow Q$, $\Gamma \rightarrow X$ and $\Gamma \rightarrow P$.
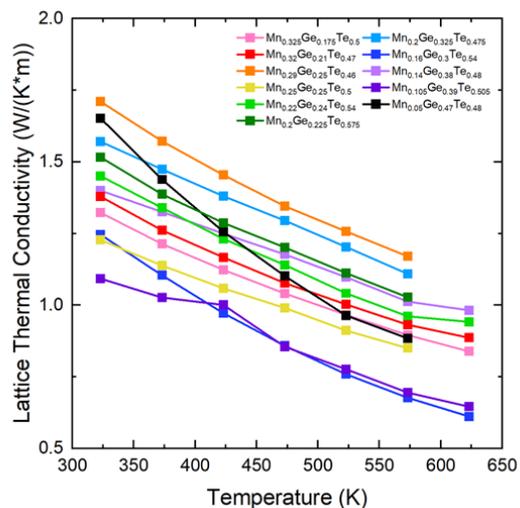
Fig. 9 Lattice thermal conductivity values decrease with increasing temperature as a result of phonon-phonon scattering.

Fig. 10 Lattice thermal conductivities along the GeTe-MnTe line decreases by roughly 50% as high fractions are Mn are incorporated into the $Ge_{1-x}Mn_xTe$ alloy.

the valence bands show flat, near dispersionless features8h). This matches well with our experimental observation of very high effective mass with a higher percentage of Mn inclusion, resulting very low mobility above 15%Mn. Optimization of the thermoelectric properties of $Ge_{1-x}Mn_xTe$ requires balancing the Ge/Mn ratio to improve band convergence while preventing the effective mass and scattering from becoming too high. We note that Mn as an alloying partner, due to its $3d$ orbitals, may be an extreme case; for example Figure 9b in the ESI shows the unfolded band structure for $Ge_{0.5}Sn_{0.5}Te$ alloy instead, which by contrast retains well-defined and less distorted valence band extrema despite the large degree of alloying.

3.5 Thermal transport and zT

Lattice thermal conductivity was determined assuming the total thermal conductivity contains only majority carrier and phononic contributions ($\kappa_{tot} = \kappa_{lattice} + \kappa_{electronic}$). The electronic component of thermal conductivity was determined using the relationships $\kappa_{electronic} = L \cdot \sigma \cdot T$, where the Lorenz number was estimated using the procedure described by Kim et al.[51]. Figure 9 shows the lattice thermal conductivity of the $Ge_{1-x}Mn_xTe$ samples decreases with increasing temperature indicating samples are dominated by phonon-phonon scattering. The samples with the lowest lattice thermal conductivities have moderate Mn percentages, putting the matrix compositions close to that of the rhombohedral to cubic transition at 21%. The structural transition point may aid in reducing the lattice thermal conductivity as samples with both lower and higher Mn/Ge ratios have lattice thermal conductivities greater than 1 W/mK at room temperature.

At 573 K, the lattice thermal conductivity values are all near or below unity in Figure 10 which is consistent with other studies on $Ge_{1-x}Mn_xTe$.[11,18] As secondary phases are present in the samples, the lattice thermal conductivity values greater than unity may be a result of elemental germanium that has a lattice thermal conductivity of ~30 W/mK at 573 K or $MnTe_2$ with a lattice
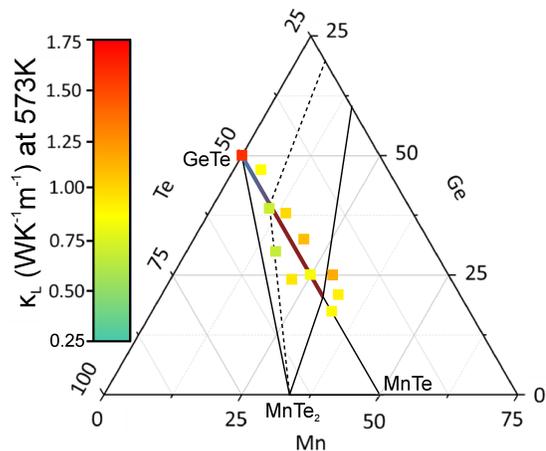
thermal conductivity of 1.2 W/mK at 500 K.[52,53] Secondary phase fractions of MnTe are unlikely to increase the lattice thermal conductivity as the values are close to or below 1 W/mK.[14]

The thermoelectric figure of merit in Figure 11 shows a spread of values ranging from 0.03~0.8 at 623 K. The highest zT sample ($Mn_{0.14}Ge_{0.38}Te_{0.48}$) has a modest lattice thermal conductivity, however, the moderate resistivity and Seebeck coefficient peak above 175 μV/K enable the high performance. Interestingly, the thermoelectric quality factor (defined as $\beta \propto \frac{\mu m^{*3/2}}{\kappa_L}$) for this sample is significantly lower than that of the most Ge rich sample, suggesting that performance in these samples may be driven by hole mobility (see ESI Figure 2). The figure of merits of this work's peak samples are found to be greater than the peak samples from literature.[11,18]

Other low-Mn concentration samples also have reasonably high zT and β despite having lattice thermal conductivity above 1 W/mK. This moderate performance is driven by mobility values remaining above 2 cm^2/Vs. In contrast, the high Mn-content samples suffer from their low mobilities (<1 cm^2/Vs) and similarly high lattice thermal conductivity values. In other words, while the high effective masses contribute to a large Seebeck coefficient, the impact on mobility overshadows this benefit. A quantitative view of these trade-offs can obtained via the thermoelectric quality factor and are shown in ESI Figure 2.

4   Summary

Alloying IV-VI semiconductors with transition metals has historically not been an effective strategy to improving thermoelectric performance. $Ge_{1-x}Mn_xTe$, however, is known to be a notable exception. This work investigates how Mn alloying alters the electronic transport properties of GeTe through complementary experimental and computational approaches. Experimental determination of the $Ge_{1-x}Mn_xTe$ phase diagram identifies a solid solution ranging between 0–60% Mn concentration, however, the solubility of Mn can be as great as 70% depending on the syn-
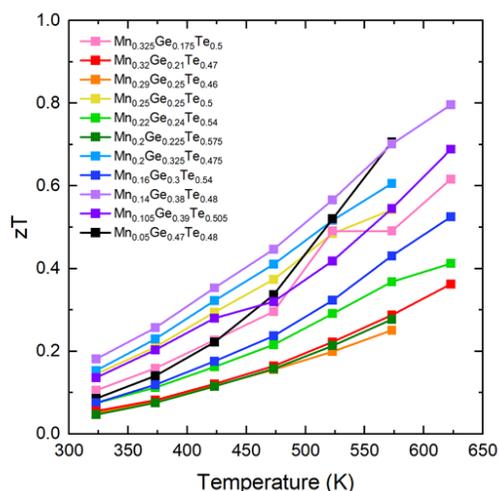
Fig. 11 Thermoelectric figure of merit peaks at moderate values of Mn while high fractions of Mn in $Ge_{1-x}Mn_xTe$ are detrimental to performance. zT in the $Ge_{1-x}Mn_xTe$ alloy occurs from a low resistivity coupled with a moderate Seebeck coefficient or a high Seebeck coefficient balanced by a moderate resistivity.

thesis temperature and cooling rate. The rhombohedral GeTe structure exists at low Mn concentrations but past 26% Mn, the $Ge_{1-x}Mn_xTe$ alloy forms in the cubic rock salt structure. Experimental measurements on samples along the alloy line find that Mn reduces the hole mobility as a result of a dramatic increase in the hole effective mass. Disordered alloy calculations along the $Ge_{1-x}Mn_xTe$ line provide an in-depth view of the electronic band structure and its the contributions to electronic transport. From the band structure calculations, it is found that moderate Mn inclusion is responsible for flattening of the Σ bands near the VBM thereby increasing the effective mass by nearly six times that of pure GeTe. Both calculations and experiment come to the agreement that moderate Mn concentration can improve thermoelectric performance but heavier concentrations of Mn negatively affect the effective mass and mobility.

Conflicts of interest

There are no conflicts to declare.

Acknowledgements

Notes and references

1 Y. Gelbstein, B. Dado, O. Ben-Yehuda, Y. Sadia, Z. Dashevsky and M. P. Dariel, Journal of Electronic Materials, 2010, **39**, 2049–2052.

2 Y. Gelbstein, J. Davidow, S. N. Girard, D. Y. Chung and M. Kanatzidis, Advanced Energy Materials, 2013, **3**, 815–820.

3 X. Zhang, Z. Bu, S. Lin, Z. Chen, W. Li and Y. Pei, Joule, 2020, **4**, 986–1003.

4 D. Wu, L. Xie, X. Xu and J. He, Advanced Functional Materials, 2019, **29**, 1806613.

5 M. Hong, Y. Wang, W. Liu, S. Matsumura, H. Wang, J. Zou and Z.-G. Chen, Advanced Energy Materials, 2018, **8**, 1801837.

6 W. Johnston and D. Sestrich, Journal of Inorganic and Nuclear Chemistry, 1961, **19**, 229–236.

7 O. G. Vendik and S. P. Zubko, Journal of Applied Physics, 2000, **88**, 5343–5350.

8 M. Li, Q. Sun, S.-D. Xu, M. Hong, W.-Y. Lyu, J.-X. Liu, Y. Wang, M. Dargusch, J. Zou and Z.-G. Chen, Advanced Materials, 2021, **33**, 2102575.

9 R. Tsu, W. E. Howard and L. Esaki, Physical Review, 1968, **172**, 779.

10 H. Okamoto, Journal of phase equilibria, 2000, **21**, 306–307.

11 Z. Zheng, X. Su, R. Deng, C. Stoumpos, H. Xie, W. Liu, Y. Yan, S. Hao, C. Uher, C. Wolverton et al., Journal of the American Chemical Society, 2018, **140**, 2673–2686.

12 Z. Liu, J. Sun, J. Mao, H. Zhu, W. Ren, J. Zhou, Z. Wang, D. J. Singh, J. Sui, C.-W. Chu et al., Proceedings of the National Academy of Sciences, 2018, **115**, 5332–5337.

13 R. Woods-Robinson, Y. Han, H. Zhang, T. Ablekim, I. Khan, K. A. Persson and A. Zakutayev, Chemical reviews, 2020, **120**, 4007–4055.

14 Y. Ren, Q. Jiang, J. Yang, Y. Luo, D. Zhang, Y. Cheng and Z. Zhou, Journal of Materiomics, 2016, **2**, 172–178.

15 Y. Ren, J. Yang, Q. Jiang, D. Zhang, Z. Zhou, X. Li, J. Xin and X. He, Journal of Materials Chemistry C, 2017, **5**, 5076–5082.

16 W. Xie, S. Populoh, K. Gałązka, X. Xiao, L. Sagarna, Y. Liu, M. Trottmann, J. He and A. Weidenkaff, Journal of Applied Physics, 2014, **115**, 103707.

17 J. Dong, F.-H. Sun, H. Tang, K. Hayashi, H. Li, P.-P. Shang, Y. Miyazaki and J.-F. Li, ACS applied materials & interfaces, 2019, **11**, 28221–28227.

18 B. Zhou, W. Li, X. Wang, J. Li, L. Zheng, B. Gao, X. Zhang and Y. Pei, Science China Materials, 2019, **62**, 379–388.

19 A. Zevalkink, D. M. Smiadak, J. L. Blackburn, A. J. Ferguson, M. L. Chabinyc, O. Delaire, J. Wang, K. Kovnir, J. Martin, L. T. Schelhas et al., Applied Physics Reviews, 2018, **5**, 021303.

20 A. D. LaLonde, T. Ikeda and G. J. Snyder, Review of Scientific Instruments, 2011, **82**, 025104.

21 S. Iwanaga, E. S. Toberer, A. LaLonde and G. J. Snyder, Review of Scientific Instruments, 2011, **82**, 063905.

22 C. Wood, A. Lockwood, A. Chmielewski, J. Parker and A. Zoltan, Review of scientific instruments, 1984, **55**, 110–113.

23 A. A. Coelho, Journal of Applied Crystallography, 2018, **51**, 210–218.

24 A. Zunger, S.-H. Wei, L. G. Ferreira and J. E. Bernard, Physical Review Letters, 1990, **65**, 353–356.

25 A. van de Walle, M. Asta and G. Ceder, Calphad, 2002, **26**, 539–553.

26 A. van de Walle, P. Tiwary, M. de Jong, D. Olmsted, M. Asta, A. Dick, D. Shin, Y. Wang, L.-Q. Chen and Z.-K. Liu, Calphad, 2013, **42**, 13–18.

27 J. P. Perdew, K. Burke and M. Ernzerhof, Physical Review Letters, 1996, **77**, 3865–3868.

28 G. Kresse and J. Furthmüller, Physical Review B, 1996, **54**, 11169–11186.

29 P. E. Blöchl, Physical Review B, 1994, **50**, 17953–17979.

30 M. Chakraborty, P. Pal and B. R. Sekhar, Solid State Communications, 2008, **145**, 197–200.

31 B. Bouadjemi, S. Bentata, A. Abbad and W. Benstaali, Solid State Communications, 2015, **207**, 9–15.

32 S. Ohno, K. Imasato, S. Anand, H. Tamaki, S. D. Kang, P. Gorai, H. K. Sato, E. S. Toberer, T. Kanno and G. J. Snyder, Joule, 2018, **2**, 141–154.

33 C. M. Crawford, B. R. Ortiz, P. Gorai, V. Stevanovic and E. S. Toberer, Journal of Materials Chemistry A, 2018, **6**, 24175–24185.

34 B. R. Ortiz, K. Gordiz, L. C. Gomes, T. Braden, J. M. Adamczyk, J. Qu, E. Ertekin and E. S. Toberer, Journal of Materials Chemistry A, 2019, **7**, 621–631.

35 M. Wood, M. Y. Toriyama, S. Dugar, J. Male, S. Anand, V. Stevanović and G. J. Snyder, Advanced Energy Materials, 2021, **11**, 2100181.

36 J. Male, M. T. Agne, A. Goyal, S. Anand, I. T. Witting, V. Stevanović and G. J. Snyder, Materials Horizons, 2019, **6**, 1444–1453.

37 R. Landauer, AIP Conference Proceedings, 1978, pp. 2–45.

38 C.-H. LEUNG and L. H. Van Vlack, Journal of the American Ceramic Society, 1979, **62**, 613–616.

39 C. Griffiths, Journal of Materials Science, 1978, **13**, 513–518.

40 M. Zhou, Z. M. Gibbs, H. Wang, Y. Han, C. Xin, L. Li and G. J. Snyder, Physical Chemistry Chemical Physics, 2014, **16**, 20741–20748.

41 Y. Pei, A. LaLonde, S. Iwanaga and G. J. Snyder, Energy & Environmental Science, 2011, **4**, 2085–2089.

42 S. D. Kang and G. J. Snyder, arXiv preprint arXiv:1710.06896, 2017.

43 G. J. Snyder, A. H. Snyder, M. Wood, R. Gurunathan, B. H. Snyder and C. Niu, Advanced Materials, 2020, **32**, 2001537.

44 U. V. Waghmare, N. A. Spaldin, H. C. Kandpal and R. Seshadri, Physical Review B, 2003, **67**, 125111.

45 Z. Liu, J. Sun, J. Mao, H. Zhu, W. Ren, J. Zhou, Z. Wang, D. J. Singh, J. Sui, C.-W. Chu and Z. Ren, Proceedings of the National Academy of Sciences, 2018, **115**, 5332–5337.

46 V. Popescu and A. Zunger, Phys. Rev. B, 2012, **85**, 085201.

47 P. V. C. Medeiros, S. Stafström and J. Björk, Phys. Rev. B, 2014, **89**, 041407.

48 P. V. C. Medeiros, S. S. Tsirkin, S. Stafström and J. Björk, Phys. Rev. B, 2015, **91**, 041116.

49 J. Li, X. Zhang, Z. Chen, S. Lin, W. Li, J. Shen, I. T. Witting, A. Faghaninia, Y. Chen, A. Jain, L. Chen, G. J. Snyder and Y. Pei, Joule, 2018, **2**, 976–987.

50 A. S. Gunder, C. Paillard, A. Pandit, R. Haleoot, L. Bellaiche and B. Hamad, The European Physical Journal B, 2021, **94**, year.

51 H.-S. Kim, Z. M. Gibbs, Y. Tang, H. Wang and G. J. Snyder, APL Materials, 2015, **3**, 041506.

52 Y. Xu, W. Li, C. Wang, Z. Chen, Y. Wu, X. Zhang, J. Li, S. Lin, Y. Chen and Y. Pei, Journal of Materiomics, 2018, **4**, 215–220.

53 C. J. Glassbrenner and G. A. Slack, Physical Review, 1964, **134**, A1058.